photonics

MDPI

Article

Characterization and Optimization of the Biplane Distance in Three-Dimensional Single-Molecule Localization Microscopy

Xiangyu Wang [1], Can Wang [1,2], Xi Chen [1], Tun Cao [1] and Donghan Ma [1,*]

[1] School of Optoelectronic Engineering and Instrumentation Science, Dalian University of Technology, Dalian 116024, China; wangxy0903@mail.dlut.edu.cn (X.W.); wangc2723@mail.dlut.edu.cn (C.W.); chenxi@mail.dlut.edu.cn (X.C.); caotun1806@dlut.edu.cn (T.C.)
[2] School of Biomedical Engineering, Faculty of Medicine, Dalian University of Technology, Dalian 116024, China
* Correspondence: madonghan@dlut.edu.cn

Abstract

Biplane single-molecule localization microscopy (SMLM) enables three-dimensional (3D) super-resolution imaging by extracting the axial position of fluorophores from a pair of emission patterns detected at two axially separated planes. The separation between these two imaging planes, termed the biplane distance, is a key parameter that determines axial localization precision, yet a systematic investigation of its optimal selection remains lacking. Here, we calculate the theoretical localization precision across a range of biplane distances and identify an optimal value, construct a tunable biplane detection module and experimentally evaluate axial localization precision at three different biplane distances using both fluorescent beads and biological specimens. Experimental results confirm the theoretical predictions and provide a practical framework for optimizing the biplane distance in 3D-SMLM systems.

Keywords: single-molecule localization microscopy; super-resolution microscopy; three-dimensional imaging; biplane configuration

1. Introduction

Single-molecule localization microscopy (SMLM) [1–3] enables super-resolution imaging by precisely localizing stochastically activated fluorophores through their isolated point spread functions (PSFs) and reconstructing the final image by accumulating thousands to millions of localized positions [4–6]. Originally developed for two-dimensional (2D) imaging, SMLM has been successfully extended to three dimensions (3D) based on the principle of encoding the axial position of individual molecules into measurable features of the emission patterns [7–13]. Notable examples include the astigmatic PSF [8], which introduces a cylindrical lens to induce ellipticity variations with defocus; the double-helix PSF [9], which generates two rotating lobes whose angular orientation varies linearly with axial position; and the tetrapod PSF [11], which produces a complex, multi-dot pattern enabling an extended axial range. Another distinct approach is the biplane configuration [7], where a pair of PSFs from the same emitter is detected at two axially separated planes, allowing the axial position to be determined from the resulting two patterns. Among these methods, the biplane PSF offers a unique combination of advantages: it avoids the need for complex phase masks, uses a simple and robust optical design based on a non-polarizing beam splitter, and maintains standard PSF shapes for high-precision 3D localization. This method has been widely adopted in 3D-SMLM, providing unprecedented insights into cellular structures [14,15], protein distributions [16,17], and tissue architectures [18,19].

Check for updates

Received: 12 April 2026
Revised: 2 May 2026
Accepted: 5 May 2026
Published: 8 May 2026

Copyright: © 2026 by the authors. Licensee MDPI, Basel, Switzerland. This article is an open access article distributed under the terms and conditions of the Creative Commons Attribution (CC BY) license.

In biplane SMLM, the axial separation between the two imaging planes, commonly termed the biplane distance, is typically set within the range of 0.2–1.0 μm. Intuitively, an excessively large separation causes severe defocus in one channel, degrading the signal-to-background ratio (SBR), whereas an overly small separation provides insufficient disparity between the two PSFs for reliable axial localization. Therefore, an optimal biplane distance should exist that balances these two competing effects.

Tahmasbi et al. developed a general theoretical framework for designing focal plane spacing in multifocal-plane microscopy, with an emphasis on scenarios such as strong coupling and weak coupling to balance localization accuracy and imaging depth [20]. Nevertheless, this work was intended as a general design guideline for multifocal systems rather than a dedicated study of biplane distance optimization in the context of 3D-SMLM. Moreover, the proposed method was not experimentally validated. Consequently, a systematic investigation into the optimal selection of the biplane distance in 3D-SMLM, which integrates both theoretical analysis and experimental validation, remains lacking.

In this study, we conduct a comprehensive investigation into the influence of biplane distance on axial localization precision in 3D-SMLM. We first analyze its theoretical impact and derive the optimal biplane distance under both ideal and aberrated conditions, and we then experimentally validate these findings by evaluating axial precision at different biplane distances using both fluorescent beads and biological samples.

2. Methods

2.1. Calculation of Cramér-Rao Lower Bound

According to scalar diffraction theory, the PSF can be derived from the Fourier transform of the pupil function as

$$\mu_0(x, y, z) = \left| FT\left[P\left(k_x, k_y\right) \exp(i2\pi k_z z)\right]\right|^2, \tag{1}$$

where $\mu_0(x, y, z)$ denotes the PSF at position (x, y, z) in sample space and FT is the Fourier transform. $P\left(k_x, k_y\right)$ is the pupil function with its aperture constrained by

$$k_x^2 + k_y^2 \leq (\mathrm{NA}/\lambda)^2, \tag{2}$$

where NA is the numerical aperture of the objective lens and λ is the emission wavelength in air. The factor $\exp(i2\pi k_z z)$ describes the defocus phase, where $k_z = \sqrt{(n/\lambda)^2 - k_x^2 - k_y^2}$ and n is the refractive index of the immersion medium. The pupil function can be expressed as

$$P\left(k_x, k_y\right) = A\left(k_x, k_y\right) \exp\left[i\phi\left(k_x, k_y\right)\right], \tag{3}$$

where $A\left(k_x, k_y\right)$ and $\phi\left(k_x, k_y\right)$ are the magnitude and phase of the electric field at the pupil plane, respectively. The phase can be further described as

$$\phi\left(k_x, k_y\right) = \sum_{i=1}^{N_z} c_i Z_i\left(k_x, k_y\right), \tag{4}$$

where $Z_i\left(k_x, k_y\right)$ is the i-th Zernike polynomial, c_i is its corresponding coefficient, and N_z is the number of Zernike polynomials. The final PSFs are defined as $\mu = \mu_0 I + bg$, where I is the total photon count, and bg is the background count.

For biplane SMLM, the Fisher information matrix can be simplified by assuming Poisson-distributed photon counts per pixel and applying Stirling's approximation, leading to the form reported in [20–22]

$$I_{ij}(\theta) = \sum_{m=1}^{2} \sum_{k=1}^{N_m} \frac{1}{\mu_{m,k}(\theta)} \frac{\Delta\mu_{m,k}(\theta)}{\Delta\theta_i} \frac{\Delta\mu_{m,k}(\theta)}{\Delta\theta_j}, \tag{5}$$

where $\mu_{m,k}(\theta)$ is the PSF at the k-th pixel in the m-th plane, $\theta = \{x, y, z, I, bg\}$ is the parameter vector, and N_m is the pixel count in the m-th plane. The Cramér-Rao lower bound (CRLB) characterizes the best possible estimation precision for each parameter, as expressed by

$$\mathrm{var}(\theta_i) \geq \left[I(\theta)^{-1} \right]_{ii}. \tag{6}$$

In our calculations, NA was set to 1.35 and λ was set to 0.68 μm according to experimental conditions. Each subregion consisted of 32 × 32 pixels, resulting in a total of 1024 pixels. For numerical derivative calculations, the step sizes Δx and Δy were set to 0.1 pixels, while Δz was set to 0.01 μm. To isolate the analysis from the effect of photon count, I was set to 1 and bg was set to 10^{-6}, consistent with the settings in Ref. [23].

2.2. Experimental Setup and Adjustment of Biplane Distance

A custom-designed biplane detection module was developed and integrated into a wide-field fluorescence microscope to enable 3D-SMLM imaging (Figure 1a) [24]. A 640 nm laser (LWRL640-10W-FCD, Laserwave, Beijing, China) was directed through a dichroic mirror (Di03-R405/488/561/635-t1, Semrock, Rochester, NY, USA) and focused onto the back focal plane of the objective lens (UPLSAPO100XS, Olympus, Tokyo, Japan) for sample excitation. The emitted fluorescence signal was magnified by relay lenses, modulated by a deformable mirror (Multi-3.5, Boston Micromachines, Cambridge, MA, USA), and spectrally cleaned up with an emission filter (BLP01-664R, Semrock) before entering the biplane module. Axial scanning of the objective lens was performed via a piezoelectric nano-positioning stage (ND72Z2LAQ, Physik Instrumente, Karlsruhe, Germany), while data were acquired with an sCMOS camera (C13440-20CU, Hamamatsu, Hamamatsu City, Japan) at an effective pixel size of 118 nm.

The biplane detection module was constructed using a beam splitter (BS013, Thorlabs, Newton, NJ, USA), two planar mirrors (BB1-E02, Thorlabs), and a right-angle mirror (47-005, Edmund Optics, Barrington, NJ, USA). To precisely adjust the biplane distance (Figure 1b), mirror M5 (Figure 1c) was mounted on a translation stage (LNR25M/M, Thorlabs) equipped with a piezo inertia actuator (PIA13, Thorlabs), offering an axial travel range of 13 mm with a resolution of 30 nm. To maintain the channel symmetry on the camera sensor (Figure 1d), the yaw adjustment knob of M5 was replaced with a second piezo inertia actuator (PIAK10, Thorlabs), providing a 10 mm travel range. Both actuators were connected to a centralized controller (KIM101, Thorlabs), enabling computer-controlled remote adjustment.

It should be noted that the high-precision actuators employed in this study allow for quantitative and convenient adjustment of the biplane distance after the setup has been packaged. Nevertheless, such tools are not a prerequisite. Comparable results can be obtained using manual stages and knobs at a substantially reduced cost, provided that remote adjustment capability is not required.

Before experimental validation, spherical aberrations were first minimized by adjusting the objective correction collar, and PSF optimization was then performed using the deformable mirror placed at the conjugate pupil plane in the emission path. A modal-based wavefront sensing approach [24] was employed with a fluorescent bead sample. The proce-

dure began by selecting several mirror modes of the deformable mirror and scanning their amplitudes from −5 to +5 $\lambda/2\pi$ while recording the corresponding in-focus PSFs at each step. For each captured PSF, the symmetry center was identified using the radial symmetry method [25]. A symmetric 2D Gaussian was then generated at this center and multiplied with the original PSF to form a Gaussian-masked image, whose integrated intensity served as the quality metric. The amplitude that maximized this metric was determined for each mode through Gaussian fitting. These optimal amplitudes were subsequently applied to the deformable mirror to generate an updated correction map, and the entire cycle was repeated until the output amplitudes converged. This procedure effectively suppressed instrumentation-induced aberrations, ensuring that the comparison across different biplane distances was conducted under near-aberration-free conditions.

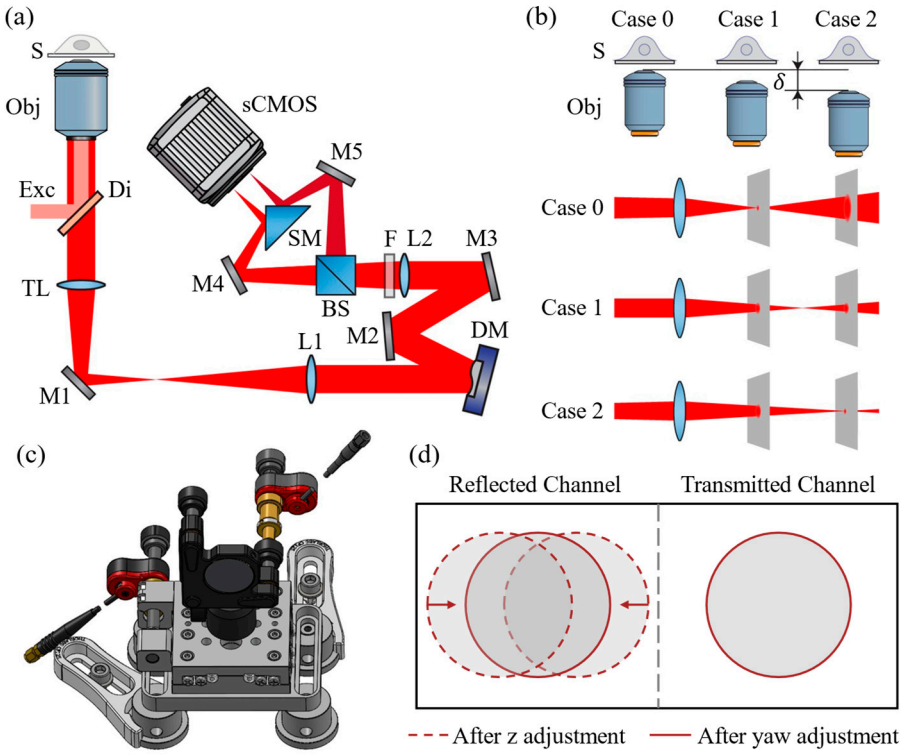

Figure 1. Biplane module in 3D-SMLM setup. (**a**) Simplified setup diagram. BS: beam splitter; Di: dichroic mirror; DM: deformable mirror; Exc: excitation; F: filter; L: lens; M: mirror; Obj: objective lens; S: sample; SM: right-angle mirror; TL: tube lens. (**b**) Definition of biplane distance δ. (**c**) Mounting method of M5. (**d**) Channel symmetry on the camera sensor.

2.3. Measurement of Biplane Distance

The biplane distance was measured by imaging a PSF stack of a fluorescent bead with a step size of 0.1 µm over an axial range of ±1.5 µm. For each PSF in each imaging plane, the intensity profiles across different axial positions were fitted with a 2D Gaussian function:

$$\mu(x,y) = I_0 \exp\left[-\frac{(x-x_0)^2+(y-y_0)^2}{2\sigma^2}\right] + bg, \tag{7}$$

where (x_0, y_0) denotes the center of the PSF, I_0 is the peak intensity, bg is the background, and σ is the standard deviation corresponding to the PSF width. For the two imaging planes, a cubic spline fit was applied to the estimated σ values and their corresponding z coordinates to generate a smooth curve. The axial positions z_1 and z_2 at which σ attained its minimum were then determined, and the biplane distance was calculated as $\delta = |z_1 - z_2|$ (Figure 2).

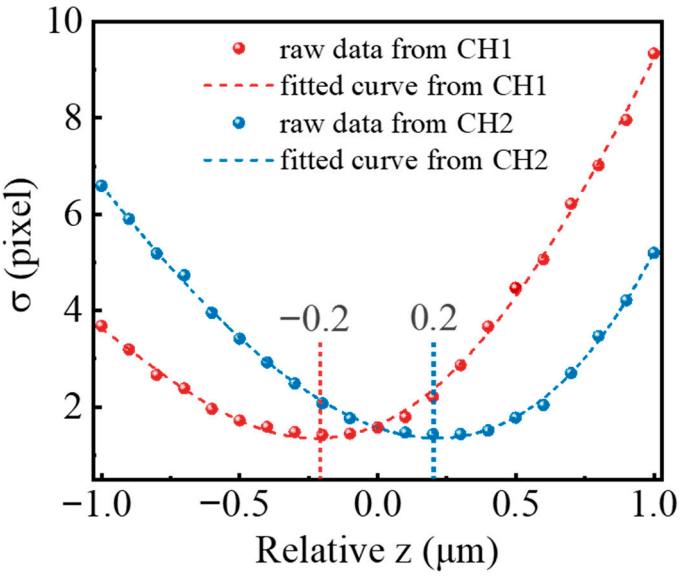

Figure 2. Determination of biplane distance.

In our experiments, the biplane distance was adjusted to approximately 0.20 μm, 0.38 μm, or 0.60 μm. In each condition, data were collected in 9 groups, with 15 PSFs uniformly sampled from each group for measurement. For quantitative evaluations, three statistical metrics were employed: the overall mean, the between-group standard deviation, and the overall standard deviation. The overall mean $\bar{\delta}$ characterizes the central tendency of all observed data, defined as

$$\bar{\delta} = \frac{1}{N_t}\sum_{i=1}^{N_g}\sum_{j=1}^{N_o}\delta_{ij}, \tag{8}$$

where δ_{ij} represents the j-th observation in the i-th group and N_t is the total number of observations. The between-group standard deviation s_b reflects the dispersion of group means around the overall mean, defined as

$$s_b = \sqrt{\frac{1}{N_g - 1}\sum_{i=1}^{N_g}\left(\bar{\delta}_i - \bar{\delta}\right)^2}, \tag{9}$$

where $\bar{\delta}_i$ denotes the mean of the i-th group. The overall standard deviation s_t describes the total dispersion of all observations about the overall mean, defined as

$$s_t = \sqrt{\frac{1}{N_t - 1}\sum_{i=1}^{N_g}\sum_{j=1}^{N_o}\left(\delta_{ij} - \bar{\delta}\right)^2}. \tag{10}$$

2.4. Measurement of Axial Localization Precision

The axial localization precision was measured by imaging a PSF stack of a fluorescent bead with a step size of 0.1 μm over an axial range of ±1.0 μm. For each bead, the axial positions were determined using our custom-developed INSPR software [15], denoted as z_i. Since the actual axial positions were spaced at 0.1 μm intervals, a linear fit was performed between the localized positions and the actual positions with the slope constrained to 1, to obtain the fitted positions $\hat{z}_i$.

The residual sum of squares (RSS) is defined as

$$\mathrm{RSS} = \sum_{i=1}^{N_l}\left(z_i - \hat{z}_i\right)^2, \tag{11}$$

and the total sum of squares (TSS) is defined as

$$\mathrm{TSS} = \sum_{i=1}^{N_l} (z_i - \bar{z})^2, \tag{12}$$

where $\bar{z}$ is the mean position calculated as $\bar{z} = \sum_{i=1}^{N_l} z_i / N_l$, and N_l is the number of localized points. The coefficient of determination R^2 is then calculated as

$$R^2 = 1 - \frac{\mathrm{RSS}}{\mathrm{TSS}}. \tag{13}$$

Furthermore, since N_l and the total photon count I can vary across different beads, and given that localization precision scales inversely with the square root of the photon count [5], a corrected residual error (CRE) enables comparison of localization precision among different biplane distances, defined as

$$\mathrm{CRE} = \sqrt{\frac{1}{N_l} \sum_{i=1}^{N_l} (z_i - \hat{z}_i)^2} \cdot \sqrt{\bar{I}}, \tag{14}$$

where $\bar{I}$ represents the mean photon count across all the localized points for the same bead.

2.5. Sample Preparation and Data Acquisition

Fluorescent bead samples were prepared as follows: a coverslip (CG15XH1, Thorlabs) was cleaned with ethanol and deionized water three times, and then blow-dried with nitrogen. 80 µL of poly-L-lysine solution (C0313, Beyotime, Shanghai, China) was incubated on the coverslip for 20 min, after which it was rinsed three times with phosphate-buffered saline (PBS, C0221A, Beyotime). A suspension of 200-nm-diameter beads was prepared by diluting the stock (T7280, Invitrogen, Carlsbad, CA, USA) 1:100 in PBS to a final volume of 100 µL. This suspension was deposited onto the coverslip for 20 min, followed by three PBS washes. The coverslip was then placed into the sample holder, 20 µL of PBS was added onto its surface, and a second cleaned coverslip was placed on top. This coverslip sandwich was sealed with two-component silicone dental glue (Hydrosil, Siladent, Goslar, Germany).

Biological samples were prepared as follows: HeLa cells were cultured on coverslips placed in a six-well chamber until they reached the desired confluence and were then fixed for 15 min with 37 °C pre-warmed PBS containing 3% paraformaldehyde (PFA, P1110, Solarbio, Beijing, China) and 0.5% glutaraldehyde (GA, P1126, Solarbio). After fixation, cells were washed twice with PBS. Blocking was performed with PBS containing 3% bovine serum albumin (BSA, abs9156, Absin, Shanghai, China) and 0.2% Triton X-100 (TX-100, X100, Sigma-Aldrich, Saint Louis, MO, USA) for 30 min at room temperature (RT). Antibodies were diluted 1:500 in PBS containing 1% BSA and 0.2% TX-100. The primary antibody (ab78547, Abcam, Cambridge, UK) was incubated with cells overnight at 4 °C, followed by three 5-min washes in PBS containing 0.05% TX-100. The secondary antibody (A21245, Invitrogen) was incubated with cells for 4 h at RT, followed by three 5-min washes in PBS containing 0.05% TX-100. Subsequently, cells were post-fixed with PBS containing 4% PFA for 10 min, washed three times with PBS, and stored in PBS at 4 °C until further use.

Immediately before imaging, the imaging buffer [26] was prepared with the following composition: 100 mM cysteamine hydrochloride (MEA, M6500, Sigma-Aldrich), 270 units/mL glucose oxidase (G2133, Sigma-Aldrich), 2400 units/mL catalase (C30, Sigma-Aldrich), 10% glucose (G7021, Sigma-Aldrich), 50 mM Tris-HCl (BL538A, Biosharp, Beijing, China), and 10 mM NaCl (S885177, Macklin, Shanghai, China) in deionized water, adjusted to pH 8.0. The cell-containing coverslip was placed into the sample holder, 100 µL of

imaging buffer was added onto the coverslip, and a second cleaned coverslip was placed on top. This coverslip sandwich was also sealed with two-component silicone dental glue.

The data acquisition procedure for mitochondria was performed as follows: First, the sample was excited with a low-intensity laser of about 50 W/cm^2 to identify a region of interest (ROI). For focus stabilization [27], a series of bright-field reference images was collected with a step size of 0.1 μm over an axial range of ±1.0 μm. Subsequently, the laser intensity was increased to 2–6 kW/cm^2, and SMLM blinking data were recorded at a frame rate of 50 Hz, acquiring 1000 frames per cycle. After each cycle, a bright-field image was captured in real time, and its 2D correlation with the reference image stack was computed. The correlation values of the reference image with the highest correlation and its eight nearest neighbors, along with their corresponding z positions, were fitted with a cubic polynomial. The z position corresponding to the peak of the fitted curve was taken as the sample drift, which was compensated by moving the objective lens in the opposite axial direction. For each ROI, 80 cycles of SMLM data were acquired, followed by analysis using the INSPR software [15].

3. Results

3.1. Theoretical Axial Localization Precision at Different Biplane Distances

We first computed the theoretical axial localization precision, defined as the square root of the CRLB, and its mean across given axial ranges in the assumption of an ideal pupil function. Using a coarse scan, the biplane distance was varied from 0.2 μm to 1.0 μm in steps of 0.1 μm (Figure 3a,b). The results show that the mean axial precision first decreased and then increased as the biplane distance grew. For axial ranges of ±0.8 μm and ±1.0 μm, the best precision was obtained at a biplane distance of 0.4 μm. Given the 0.1 μm sampling step used in this initial scan, the optimal biplane distance was estimated to lie between 0.3 μm and 0.5 μm.

To refine the estimate, we performed the calculation again using a finer sampling step of 0.02 μm (Figure 3c,d). The same trend was observed: the mean precision first decreased and then increased with increasing biplane distance. For both the ±0.8 μm and ±1.0 μm ranges, the optimum was found at 0.38 μm. Based on these refined results, a biplane distance of 0.38 μm was selected as the optimal value.

The existence of this optimal biplane distance can be physically understood as a trade-off between axial disparity and defocus-induced blurring. If the two imaging planes are spaced too closely, the two detected PSFs remain highly similar, rendering accurate extraction of axial information difficult. Conversely, if the two imaging planes are separated too far, one PSF becomes severely defocused, spreading photons over a larger area and diminishing axial information. Thus, the optimal biplane distance emerges at an intermediate value, where the two channels provide sufficient axial disparity while avoiding excessive defocus.

We further examined the axial localization precision in the presence of astigmatism (Figure 4a) or coma aberrations (Figure 4b), two types of aberrations that commonly occur in SMLM imaging. The results indicate that under slight aberrations (i.e., with a Zernike coefficient within 0.5 $\lambda/2\pi$), the axial precision varied with biplane distance in a manner similar to the case using an ideal pupil function, consistently achieving an optimum between 0.3 μm and 0.5 μm. Since PSF optimization [24] was applied before data acquisition to minimize aberrations in our experiments, the influence of more pronounced aberrations was not considered further.

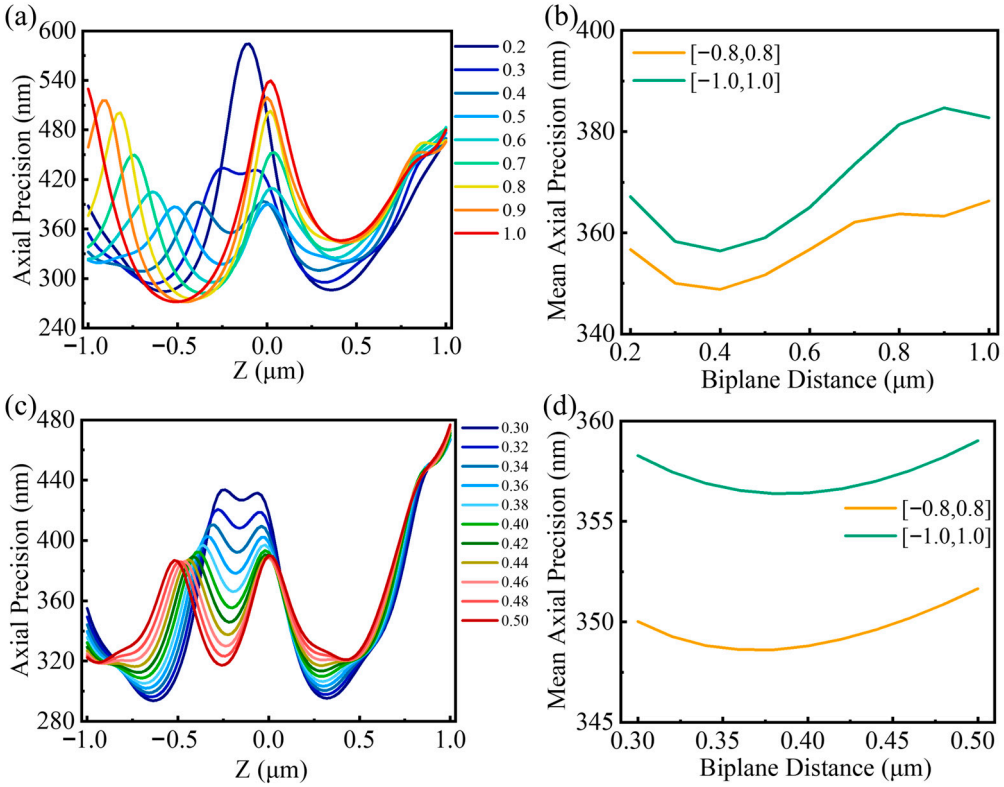

Figure 3. Theoretical axial localization precision in the assumption of an ideal pupil function. Axial precision varying with the z position (**a**) and its mean in given axial ranges (**b**) when the biplane distance was varied from 0.2 μm to 1.0 μm in steps of 0.1 μm. Axial precision varying with the z position (**c**) and its mean in given axial ranges (**d**) when the biplane distance was varied from 0.3 μm to 0.5 μm in steps of 0.02 μm. The numbers on the right side of panels (**a**,**c**) represent the biplane distances in micrometers.

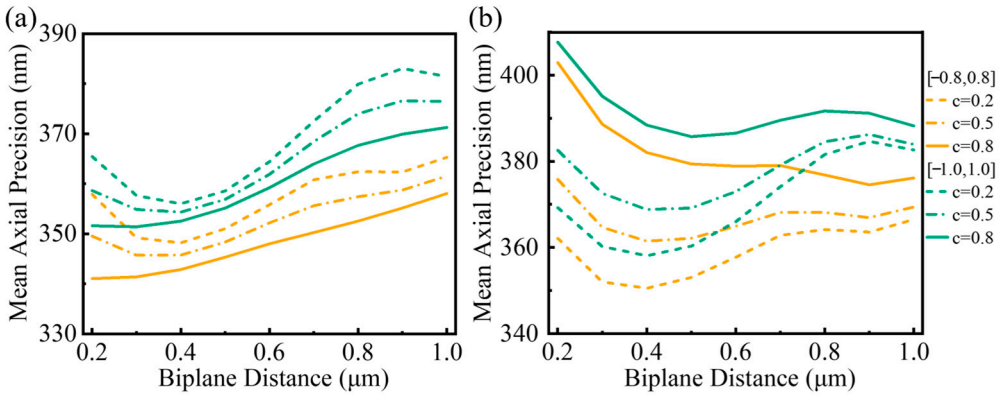

Figure 4. Theoretical axial localization precision under aberrated conditions. Mean precision across given axial range versus biplane distance in the presence of astigmatism (**a**) or coma (**b**). Dashed, dotted, and solid lines correspond to Zernike coefficients of 0.2, 0.5, and 0.8 $\lambda/2\pi$, respectively.

3.2. Measurement Results at Different Biplane Distances

Based on theoretical calculations, we set the biplane distance to approximately 0.60 μm, 0.38 μm, and 0.20 μm, and performed corresponding measurements (Figure 5a). The results (Figure 5b) indicate that the measured overall means were 0.599 μm, 0.380 μm, and 0.200 μm. The overall standard deviations were 0.013 μm, 0.011 μm, and 0.012 μm, and the between-group standard deviations were 0.015 μm, 0.011 μm, and 0.012 μm. These results demonstrate the high accuracy of the measurement method.

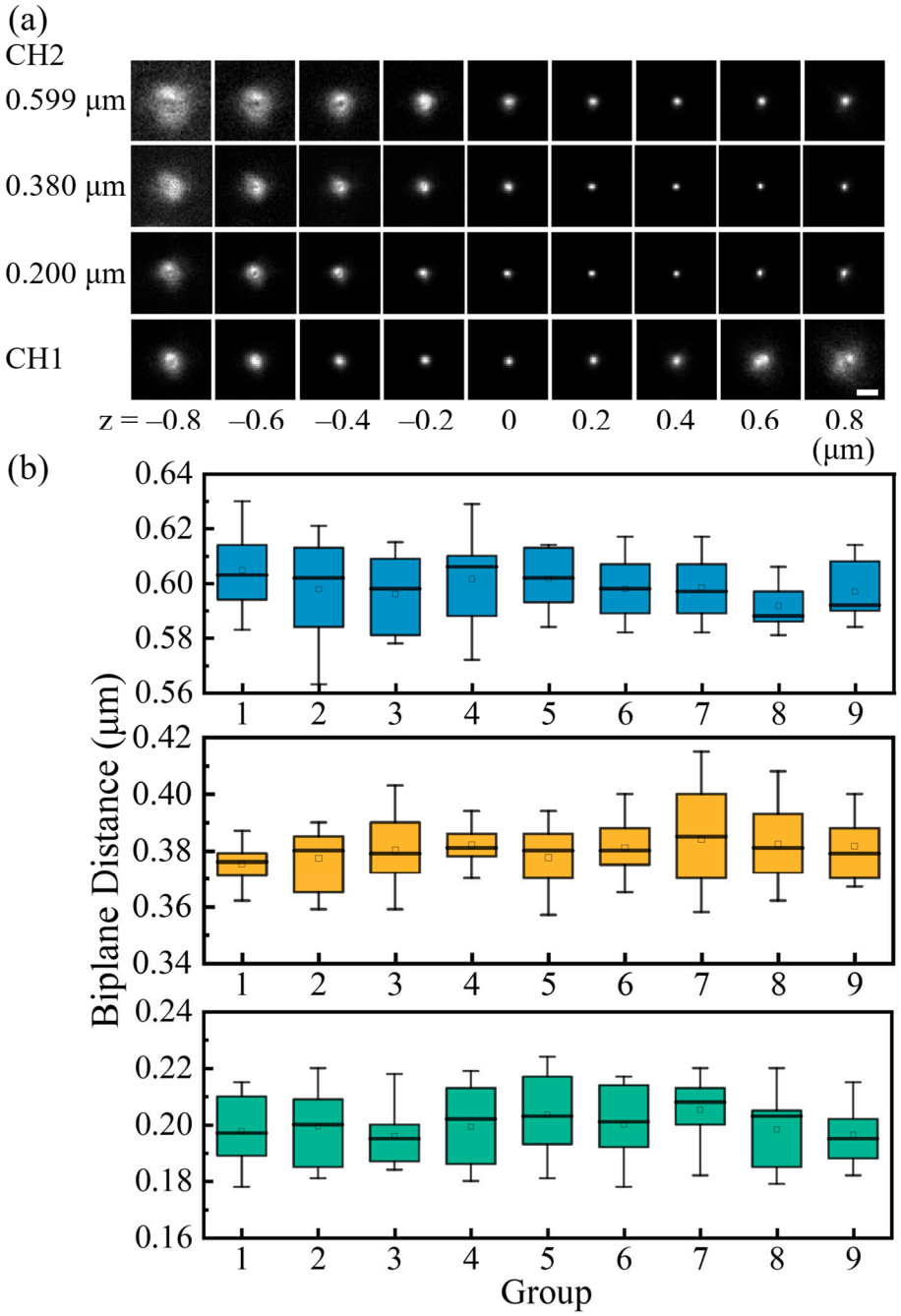

Figure 5. Measurement results at different biplane distances. (**a**) *x*-*y* PSFs acquired in two channels. (**b**) Box plot for three sets of experiments. Scale bar: 1 μm.

It should be noted that these experimentally measured biplane distances, rather than the nominal actuator displacements, were used for the subsequent analysis. This calibration step is important because the relationship between mirror displacement and the effective axial separation of the two imaging planes may be affected by optical-path geometry, alignment accuracy, and mechanical tolerances. Therefore, bead-based calibration provides a more reliable basis for comparing axial localization precision at different biplane distances.

3.3. Experimental Axial Localization Precision of Fluorescent Beads

Based on the measurement results described above, we analyzed the experimental axial localization precision using 36 fluorescent beads for each biplane distance. The results (Figure 6) show that for a biplane distance of 0.200 μm, R^2 was 0.984 ± 0.006 and CRE

was 19.98 ± 5.20 nm; for a biplane distance of 0.380 μm, R^2 was 0.991 ± 0.005 and CRE was 11.74 ± 3.69 nm; and for a biplane distance of 0.599 μm, R^2 was 0.991 ± 0.005 and CRE was 13.06 ± 3.98 nm. These findings indicate that axial precision was lowest at a biplane distance of 0.200 μm, improved at 0.599 μm, and highest at 0.380 μm. This trend is consistent with the theoretical analysis presented above, confirming that the optimal biplane distance is around 0.38 μm under our imaging conditions.

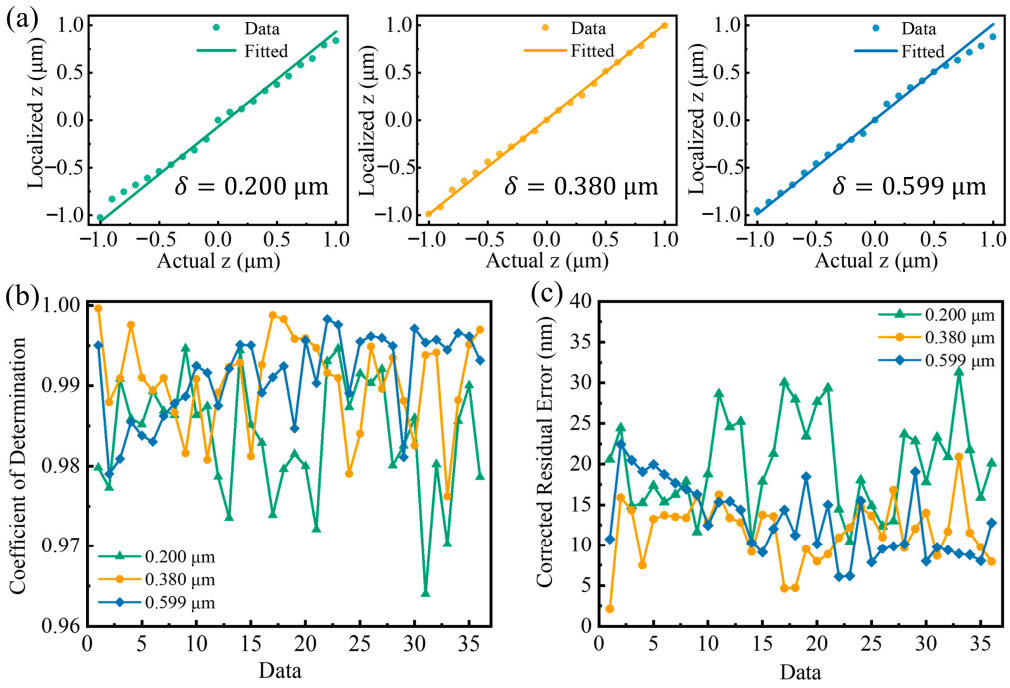

Figure 6. Experimental axial localization results of fluorescent beads. (**a**) Axial localization results for one typical bead at different biplane distances. (**b**) Distribution of coefficient of determination. (**c**) Distribution of corrected residual error.

3.4. Experimental Axial Localization Precision of Mitochondrial Samples

We further performed 3D-SMLM imaging of mitochondria at the three selected biplane distances (Figure 7). The resulting cross-sectional images reveal axial distributions with resolvable multi-peak structures, indicating spatially distinct features along the *z* axis within the sample. Notably, the annular morphologies were best resolved at a biplane distance of 0.380 μm (Figure 7b), followed by 0.599 μm (Figure 7c), where axial resolution was somewhat reduced. In contrast, localization artifacts became pronounced, and image quality was poorest at a biplane distance of 0.200 μm (Figure 7a). This trend broadly aligns with the bead-based localization results described above.

The mitochondrial imaging results should be interpreted as a practical validation of the optimized biplane distance rather than an absolute quantitative comparison of resolution. Unlike fluorescent beads, biological samples involve additional factors, including structural heterogeneity, labeling density, local background, fluorophore blinking behavior, and possible sample-induced aberrations. While these factors can influence imaging resolution, the biological imaging approach still yields meaningful and informative results. Importantly, the observation that the biplane distance of 0.380 μm produced clearer cross-sectional structures and fewer apparent localization artifacts is consistent with the bead-based measurements, thereby supporting the practical applicability of the optimized biplane distance in biological 3D-SMLM imaging.

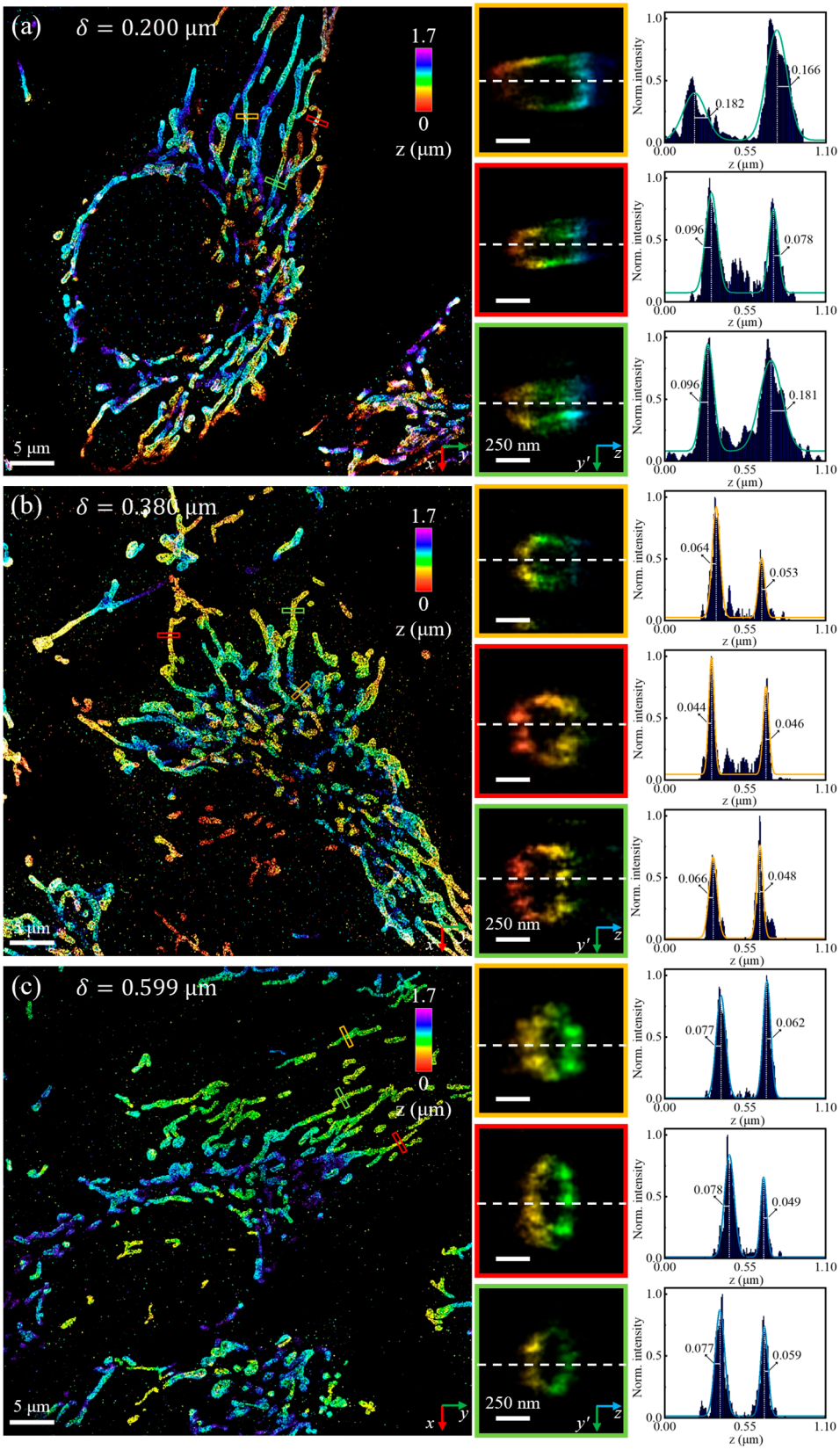

Figure 7. Super-resolution reconstruction results of mitochondria imaged at different biplane distances. Overview of the mitochondrial network (**left**), enlarged cross-sectional views of membrane contours (**middle**) corresponding to the yellow, red, and green boxed regions in the left panel, and their intensity profiles along the z direction (**right**) measured along the white dashed lines in the middle panel, at biplane distances of 0.200 μm (**a**), 0.380 μm (**b**), and 0.599 μm (**c**). The cross sections are rotated to project the 3D membrane-bounded structures onto a 2D image plane. The numbers near the black arrows in the right panels indicate σ_z in micrometers.

4. Discussion

In this study, we systematically evaluated the influence of biplane distance on axial localization precision in biplane 3D-SMLM. Both theoretical analysis and experimental validations showed that a biplane distance of 0.38 μm provided better axial localization precision than shorter or longer separations under our imaging conditions. This result demonstrates that the biplane distance is not merely a mechanical spacing parameter but also an important design factor that directly affects the axial information content of the detected PSF pair.

The present work complements previous studies on focal-plane-spacing optimization in multifocal-plane microscopy. While earlier theoretical work [20] provided general design principles for multifocal systems, our study focuses specifically on the biplane configuration in 3D-SMLM and experimentally validates the CRLB-derived prediction using both fluorescent beads and biological samples. Therefore, this work provides a practical reference for selecting the biplane distance in similar 3D-SMLM systems.

The main evaluation in this study was performed within an axial range of ±1.0 μm. Therefore, the optimized distance of 0.38 μm should not be directly generalized to thicker specimens with axial dimensions of several micrometers. For larger-volume 3D imaging, simply increasing the biplane distance may introduce excessive defocus and reduce localization precision. Alternative strategies, such as axial scanning with layer-by-layer reconstruction [15] or engineered long-axial-range PSFs such as tetrapod PSFs [11], may be more appropriate. These strategies require dedicated 3D alignment or localization models and are beyond the scope of the present biplane distance optimization.

5. Conclusions

In this study, we systematically characterized and optimized the biplane distance in biplane 3D-SMLM. Through CRLB analysis, we identified that the mean axial precision first improved and then deteriorated with increasing biplane distance, leading to an optimal value of approximately 0.38 μm within the axial range of ±1.0 μm under our imaging conditions. This prediction was experimentally validated using fluorescent beads and mitochondrial samples, where the biplane distance of 0.380 μm provided better axial localization performance than 0.200 μm and 0.599 μm. By combining theoretical analysis, tunable optical implementation, and experimental validation, this study provides a practical framework for selecting the biplane distance in 3D-SMLM. The proposed optimization strategy may further support the development of biplane imaging systems integrated with adaptive optics, engineered PSFs, or multicolor detection for more robust volumetric super-resolution imaging.

Supplementary Materials: The following supporting information can be downloaded at: https://www.mdpi.com/article/10.3390/photonics13050462/s1, Supplementary File S1: MATLAB code and source data used to generate the figures and perform the analyses presented in this study.

Author Contributions: Conceptualization, D.M.; methodology, X.W.; validation, X.W., C.W. and X.C.; writing—original draft preparation, X.W.; writing—review and editing, D.M.; visualization, X.W., C.W. and X.C.; supervision, D.M. and T.C.; funding acquisition, D.M. All authors have read and agreed to the published version of the manuscript.

Funding: State Key Laboratory of Precision Measurement Technology and Instruments (2024PMTI01); National Natural Science Foundation of China (62305041).

Data Availability Statement: The original contributions presented in this study are included in the Supplementary Materials. Further inquiries can be directed to the corresponding author.

Acknowledgments: We thank Jinbo Zhu and Lan Shao of Dalian University of Technology for their kind help in sample preparation.

Conflicts of Interest: The authors declare no conflicts of interest.

Abbreviations

The following abbreviations are used in this manuscript:

2D	Two-Dimensional
3D	Three-Dimensional
BSA	Bovine Serum Albumin
CRE	Corrected Residual Error
CRLB	Cramér-Rao Lower Bound
GA	Glutaraldehyde
MEA	Cysteamine Hydrochloride
NA	Numerical Aperture
PBS	Phosphate-Buffered Saline
PFA	Paraformaldehyde
PSF	Point Spread Function
ROI	Region of Interest
RSS	Residual Sum of Squares
RT	Room Temperature
SBR	Signal-to-Background Ratio
sCMOS	Scientific Complementary Metal-Oxide-Semiconductor
SMLM	Single-Molecule Localization Microscopy
TSS	Total Sum of Squares
TX-100	Triton X-100

References

1. Betzig, E.; Patterson, G.H.; Sougrat, R.; Lindwasser, O.W.; Olenych, S.; Bonifacino, J.S.; Davidson, M.W.; Lippincott-Schwartz, J.; Hess, H.F. Imaging intracellular fluorescent proteins at nanometer resolution. *Science* **2006**, *313*, 1642–1645. [CrossRef]
2. Hess, S.T.; Girirajan, T.P.; Mason, M.D. Ultra-high resolution imaging by fluorescence photoactivation localization microscopy. *Biophys. J.* **2006**, *91*, 4258–4272. [CrossRef]
3. Rust, M.J.; Bates, M.; Zhuang, X. Sub-diffraction-limit imaging by stochastic optical reconstruction microscopy (STORM). *Nat. Methods* **2006**, *3*, 793–796. [CrossRef]
4. Schermelleh, L.; Ferrand, A.; Huser, T.; Eggeling, C.; Sauer, M.; Biehlmaier, O.; Drummen, G.P.C. Super-resolution microscopy demystified. *Nat. Cell Biol.* **2019**, *21*, 72–84. [CrossRef]
5. Lelek, M.; Gyparaki, M.T.; Beliu, G.; Schueder, F.; Griffié, J.; Manley, S.; Jungmann, R.; Sauer, M.; Lakadamyali, M.; Zimmer, C. Single-molecule localization microscopy. *Nat. Rev. Methods Primers* **2021**, *1*, 39. [CrossRef]
6. Chen, X.; Wang, X.; Huang, F.; Ma, D. Multicolor single-molecule localization microscopy: Review and prospect. *PhotoniX* **2024**, *5*, 29. [CrossRef]
7. Juette, M.F.; Gould, T.J.; Lessard, M.D.; Mlodzianoski, M.J.; Nagpure, B.S.; Bennett, B.T.; Hess, S.T.; Bewersdorf, J. Three-dimensional sub-100 nm resolution fluorescence microscopy of thick samples. *Nat. Methods* **2008**, *5*, 527–529. [CrossRef]
8. Huang, B.; Wang, W.; Bates, M.; Zhuang, X. Three-dimensional super-resolution imaging by stochastic optical reconstruction microscopy. *Science* **2008**, *319*, 810–813. [CrossRef]
9. Pavani, S.R.P.; Thompson, M.A.; Biteen, J.S.; Lord, S.J.; Liu, N.; Twieg, R.J.; Piestun, R.; Moerner, W.E. Three-dimensional, single-molecule fluorescence imaging beyond the diffraction limit by using a double-helix point spread function. *Proc. Natl. Acad. Sci. USA* **2009**, *106*, 2995–2999. [CrossRef]
10. Aquino, D.; Schönle, A.; Geisler, C.; Middendorff, C.V.; Wurm, C.A.; Okamura, Y.; Lang, T.; Hell, S.W.; Egner, A. Two-color nanoscopy of three-dimensional volumes by 4Pi detection of stochastically switched fluorophores. *Nat. Methods* **2011**, *8*, 353–359. [CrossRef]
11. Shechtman, Y.; Sahl, S.J.; Backer, A.S.; Moerner, W.E. Optimal point spread function design for 3D imaging. *Phys. Rev. Lett.* **2014**, *113*, 133902. [CrossRef]
12. Jia, S.; Vaughan, J.C.; Zhuang, X. Isotropic 3D super-resolution imaging with a self-bending point spread function. *Nat. Photonics* **2014**, *8*, 302–306. [CrossRef]

13. Bon, P.; Linarès-Loyez, J.; Feyeux, M.; Alessandri, K.; Lounis, B.; Nassoy, P.; Cognet, L. Self-interference 3D super-resolution microscopy for deep tissue investigations. *Nat. Methods* **2018**, *15*, 449–454. [CrossRef]
14. Song, K.H.; Zhang, Y.; Wang, G.; Sun, C.; Zhang, H.F. Three-dimensional biplane spectroscopic single-molecule localization microscopy. *Optica* **2019**, *6*, 709–715. [CrossRef]
15. Xu, F.; Ma, D.; MacPherson, K.P.; Liu, S.; Bu, Y.; Wang, Y.; Tang, Y.; Bi, C.; Kwok, T.; Chubykin, A.A.; et al. Three-dimensional nanoscopy of whole cells and tissues with in situ point spread function retrieval. *Nat. Methods* **2020**, *17*, 531–540. [CrossRef]
16. Li, Y.; Shi, W.; Liu, S.; Cavka, I.; Wu, Y.L.; Matti, U.; Wu, D.; Koehler, S.; Ries, J. Global fitting for high-accuracy multi-channel single-molecule localization. *Nat. Commun.* **2022**, *13*, 3133. [CrossRef]
17. Barentine, A.E.S.; Lin, Y.; Courvan, E.M.; Kidd, P.; Liu, M.; Balduf, L.; Phan, T.; Rivera-Molina, F.; Grace, M.R.; Marin, Z.; et al. An integrated platform for high-throughput nanoscopy. *Nat. Biotechnol.* **2023**, *41*, 1549–1556. [CrossRef]
18. Albrecht, N.E.; Jiang, D.; Akhanov, V.; Hobson, R.; Speer, C.M.; Robichaux, M.A.; Samuel, M.A. Rapid 3D-STORM imaging of diverse molecular targets in tissue. *Cell Rep. Methods* **2022**, *2*, 100253. [CrossRef]
19. Zhang, P.; Ma, D.; Cheng, X.; Tsai, A.P.; Tang, Y.; Gao, H.C.; Fang, L.; Bi, C.; Landreth, G.E.; Chubykin, A.A.; et al. Deep learning-driven adaptive optics for single-molecule localization microscopy. *Nat. Methods* **2023**, *20*, 1748–1758. [CrossRef]
20. Tahmasbi, A.; Ram, S.; Chao, J.; Abraham, A.V.; Tang, F.W.; Sally Ward, E.; Ober, R.J. Designing the focal plane spacing for multifocal plane microscopy. *Opt. Express* **2014**, *22*, 16706–16721. [CrossRef]
21. Rieger, B.; Stallinga, S. The lateral and axial localization uncertainty in super-resolution light microscopy. *ChemPhysChem* **2014**, *15*, 664–670. [CrossRef] [PubMed]
22. Ober, R.J.; Ram, S.; Ward, E.S. Localization accuracy in single-molecule microscopy. *Biophys. J.* **2004**, *86*, 1185–1200. [CrossRef]
23. Fang, L.; Huang, F. Measurement precision bounds on aberrated single-molecule emission patterns. *Opt. Express* **2024**, *32*, 31431–31447. [CrossRef] [PubMed]
24. Wang, X.; Chen, X.; Wang, C.; Cao, T.; Zhang, P.; Ma, D. Precise adjustment of the three-dimensional position of the deformable mirror in adaptive optics-assisted microscopy. *Opt. Lett.* **2025**, *50*, 7500–7503. [CrossRef]
25. Parthasarathy, R. Rapid, accurate particle tracking by calculation of radial symmetry centers. *Nat. Methods* **2012**, *9*, 724–726. [CrossRef]
26. Wang, C.; Sun, Z.; Ma, D. Review of imaging buffers used in stochastic optical reconstruction microscopy. *Chin. Chem. Lett.* **2025**, *36*, 110677. [CrossRef]
27. McGorty, R.; Kamiyama, D.; Huang, B. Active microscope stabilization in three dimensions using image correlation. *Opt. Nanoscopy* **2013**, *2*, 3. [CrossRef]

Disclaimer/Publisher's Note: The statements, opinions and data contained in all publications are solely those of the individual author(s) and contributor(s) and not of MDPI and/or the editor(s). MDPI and/or the editor(s) disclaim responsibility for any injury to people or property resulting from any ideas, methods, instructions or products referred to in the content.